Title: Assessing the influence of non-uniform gas speed on the melt pool depth in laser powder bed fusion additive manufacturing

Authors: Jordan S. Weaver[1,*], Alec Schlenoff[1], David Deisenroth[1], Shawn Moylan[1]

[1] Engineering Laboratory, National Institute of Standards and Technology, Gaithersburg, MD, USA
[*] corresponding author, jordan.weaver@nist.gov

Abstract:
Purpose: This paper aims to investigate the influence of non-uniform gas speed across the build area on the melt pool depth during laser powder bed fusion. The study focuses on whether a non-uniform gas speed is a source of process variation within an individual build.

Design/methodology/approach: Parts with many single-track laser scans were printed and characterized in different locations across the build area coupled with corresponding gas speed profile measurements. Cross-sectional melt pool depth, width, and area are compared against build location/gas speed profiles, scan direction, and laser scan speed.

Findings: The study shows that the melt pool depth of single-track laser scans produced on parts are highly variable. Despite this, trends were found showing a reduction in melt pool depth for slow laser scan speeds on the build platform near the inlet nozzle and when the laser scans are parallel to the gas flow direction.

Originality/value: A unique dataset of single-track laser scan cross-sectional melt pool measurements and gas speed measurements was generated to assess process variation associated with non-uniform gas speed. Additionally, a novel sample design was used to increase the number of single-track tests per part, which is widely applicable to studying process variation across the build area.

Keywords: additive manufacturing, metals, laser plume, melt pool, gas flow

1. Introduction:

Additive manufacturing is an emerging technology that can significantly reduce lead time while allowing for more complex part designs for specific applications compared to traditional manufacturing methods. Laser powder bed fusion (LPBF) is a prevalent additive manufacturing (AM) method for metals that creates a part in a layer-by-layer process of selectively melting a bed of powder feedstock with a laser. The laser interaction with the powder and solid part creates byproducts that include the plume (evaporated metal that condenses into nanoparticles), hot spatter (material ejected from the molten pool) and cold spatter (gas/vapor entrained powder not fused to the part). These byproducts have adverse effects on the LPBF process.

The complex physics of the laser-powder interaction result in a plume comprised of suspended particles that can attenuate the laser beam via Rayleigh scattering (Greses et al., 2004) and Mie scattering (Reijonen et al., 2020). During high-power Ytterbium fiber laser welding of steel, Shcheglov et al. (Shcheglov et al., 2012) and Greses et al. (Greses et al., 2004) measured the average particle size and number density of particles in the plume. Shcheglov (Shcheglov et al.,

2012) estimated 12 % attenuation while Greses et al. (Greses et al., 2004) used a low-power probe laser to measure a worst-case scenario of 40 % attenuation. Bitharas et al. (Bitharas et al., 2021, Bitharas et al., 2022) and Bidare et al. (Bidare et al., 2018) visualized the plume during LPBF using Schlieren imaging. Depending on the laser parameters, the vapor jet in the plume was emitted forward, upward, or backward (Bidare et al., 2018). The presence of a crossflow of inert gas prevented the buildup of byproducts in the chamber atmosphere (Bidare et al., 2018, Bitharas et al., 2021). Bitharas et al. (Bitharas et al., 2021) further showed that when the flow direction was the same as the laser scan direction, the likelihood of laser-byproduct interactions increased.

The laser-byproduct interactions are believed to directly impact the process quality. Anwar and Pham (Anwar and Pham, 2017) observed that parts built with the crossflow parallel to the laser scan had lower ultimate tensile strength. The explanation is that when the laser scans in the same direction as the gas flow, byproducts are blown back into the laser, causing attenuation and/or scattering of the laser and an increase in porosity defects. This mechanism is similar to how byproducts from one laser can be blown into another laser on a multi-laser LPBF system, as studied by Tenbrock et al. (Tenbrock et al., 2021). In the worst case, with no gas flow, Deisenroth et al. (Deisenroth et al., 2020) showed that the melt pool cross-section becomes shallow and irregularly shaped compared to the same laser process conditions with directional gas flow present. This was observed on bare plate scans where the effect of spatter is minimal, and the cause for shallow, irregularly shaped melt pools is believed to be the plume. Reijonen et al. (Reijonen et al., 2020) observed similar results in experiments with powder. There was a reduction in melt pool height and an increase in melt pool width for some laser parameters under reduced gas flow speeds. They argue that beam scattering in addition to attenuation is occurring.

There is a variety of spatter byproducts generated during LPBF. Young et al. (Young et al., 2020) observed spatter during LPBF using high-speed, high-energy x-ray imaging, and characterized five types of spatter depending on the formation mechanism. Obeidi et al. (Ahmed Obeidi et al., 2020) collected and characterized the spatter, and found that it is predominantly larger, irregular particles with different surface chemistry and density compared to the feedstock powder. Nasar et al. (Nassar et al., 2019) used high-speed videos to observe the formation of large agglomerates by inelastic collisions of spatter, and they observed that these agglomerates can interfere with the laser track geometry (viewed from the top surface). The spatter byproducts create further problems in the LPBF process when they land on the powder bed or parts.

Ladewig et al. (Ladewig et al., 2016) observed that decreasing cross-flow gas speed led to more redeposition of byproducts on parts and the surrounding powder bed. Esmaeilizadeh et al. (Esmaeilizadeh et al., 2019) observed a spatter-rich region in the build area near the outlet side (downstream). The crossflow sends some spatter downstream without reaching the outlet. The spatter-rich region in the build area correlated with an increase in porosity defects. Berez et al. (Berez et al., 2022) showed that the fatigue life depended on the location of parts on the build plate. Lower fatigue life and more porosity defects were more likely to occur near the outlet side of the build area (downstream). Moran et al. (Moran et al., 2021) also observed increased porosity near the outlet for one LPBF machine. However, they observed the opposite trend on a different LPBF machine, with more porosity defects near the inlet side of the build area. In the later observation, a computational fluid dynamic (CFD) model of the directional gas flow revealed a laminar eddy in the region near the inlet. It's unclear if spatter or the plume or both caused the increase in porosity in the upstream region.

It is clear that a critical function in the LPBF process is the removal of byproducts (or a significant portion of them). This is achieved by circulating inert gas through the build chamber. The inert gas flow (and thus byproduct removal) may differ between LPBF machines and even across the build platform within one machine. Anwar and Pham (Anwar and Pham, 2017) observed that increasing the gas speed by 30% increased the ultimate tensile strength. Shen et al. (Shen et al., 2020) and Reijonen et al. (Reijonen et al., 2020) showed that increasing the gas speed reduces porosity defects. These observations are in line with those from previous authors that saw better byproduct removal with increasing cross-flow speed. Shen et al. (Shen et al., 2020) also found an upper limit on gas speed occurs when the powder bed is disturbed by the gas flow. In addition to the average speed, uniformity across the build platform is important. Ferrar et al. (Ferrar et al., 2012) showed that creating more uniform gas flow across the build area reduced the standard deviation in mechanical properties.

Very few studies that focused on gas flow and byproduct removal in LPBF have reported melt pool cross-sections, although they are arguably a fundamental measurement of the LPBF process. Reijonen et al. (Reijonen et al., 2020) measured the melt pool width and depth for different nominal gas speeds and laser power and speed combinations. Recent work by Weaver et al. (Weaver et al., 2021) revealed that the speed profiles (speed versus height from the recoating plane) across the build platform can be significantly different. In this study, we aim to understand how the non-uniformity in gas speed under nominally optimized gas speed settings may create variations in the melt pool size. To this end, single-track laser scans were produced during the building process at different locations on the build platform and with different laser process parameters. Cross-sectional measurements of the single tracks were made using optical microscopy.

2. Methods

Experiments were carried out on an EOS[1] M290 machine with virgin EOS Nickel alloy 625 (IN625) powder (lot number M341901). According to the mill test certificate, the particle size distribution was d10 = 19 µm, d50 = 32 µm, and d90 = 50 µm measured via laser diffraction. The default laser process parameters were used on all parts with the exception of single-track laser scans. Three different laser scan speeds were used for single-track laser scans, including the default value of 960 mm s^{-1}. The main process parameters are given in Table 1. Thirty 20 mm × 20 mm blocks were distributed throughout the build area as shown in Figure 1. At each location, the laser scans were either aligned with the Y-direction (up and down from a top-view) or aligned with the X-direction (left and right from a top-view) as indicated by the arrows. Two

[1] Certain commercial equipment, instruments, or materials are identified in this paper in order to specify the experimental procedure adequately. Such identification is not intended to imply recommendation or endorsement by NIST, nor is it intended to imply that the materials or equipment identified are necessarily the best available for the purpose

different sample designs were used: top layer and multi-layer. The top layer sample has a 7 mm height base with three rectangular regions on top that are a single layer height (0.04 mm). Inside these three rectangular regions, the hatch spacing was increased to 2 mm so that only three to four tracks with 2 mm spacing were printed. The scans alternated directions (either up and down or left and right) within each region. Each region was also assigned a different laser scan speed according to Table 1. The multi-layer sample had a total height of 11 mm. It contained thirty-six internal, triangular channels. The triangular channels can be reliably printed without support structures. Inside each channel on the bottom surface is a rectangle with a 1 mm width and a single-layer height. A contour scan strategy that followed the rectangle perimeter was used to create tracks scanning alternate directions inside channels. The short sides of the rectangle were ignored. Thus, single tracks with 1 mm spacing were printed also at three different laser scan speeds. Additional details for the tracks on each sample are given in Appendix A. Upskin scanning parameters were left on for the main parts. In other words, the single tracks were created after spreading a single layer of powder on top of an upskin surface. The upskin creates a smoother surface by scanning the surface multiple times with reduced powder and increased speed in different directions. This also reduces any influence the prior layer scan pattern may have on a single track that is printed on the next layer. More details on the printing parameters of the base material are provide in Appendix B. All of the samples were removed from the build platform and cross-sectioned perpendicular to the single tracks in the approximate middle. The top layer samples without internal features allowed for hardness measurements (not included in this study), while the multi-layer samples allowed for many more tracks per sample. The positions of samples were chosen to match the positions of gas speed measurements in Ref. (Weaver et al., 2021). The layout was chosen to study the non-uniform speed profiles along the Y-direction. Hence, both sample types and scan directions exist at each Y-position. Samples were printed from left to right starting with the row closest to the outlet and ending at the row closest to the inlet (i.e., from sample 30 to 1).

Table 1. Main LPBF process parameters. The standard nozzle type has a grate of circular holes compared to the grid nozzle that has a grate of rectangular channels. A hard, ceramic recoating blade was used.

Laser Power (W)	Laser scan speed (mm s^{-1})	Hatch spacing (mm)	Stripe Width (mm)	Layer thickness (mm)	Inert gas	Nozzle Type
285	300 / 960 /1200	0.11	10	0.04	Argon, < 0.1 % oxygen	Standard

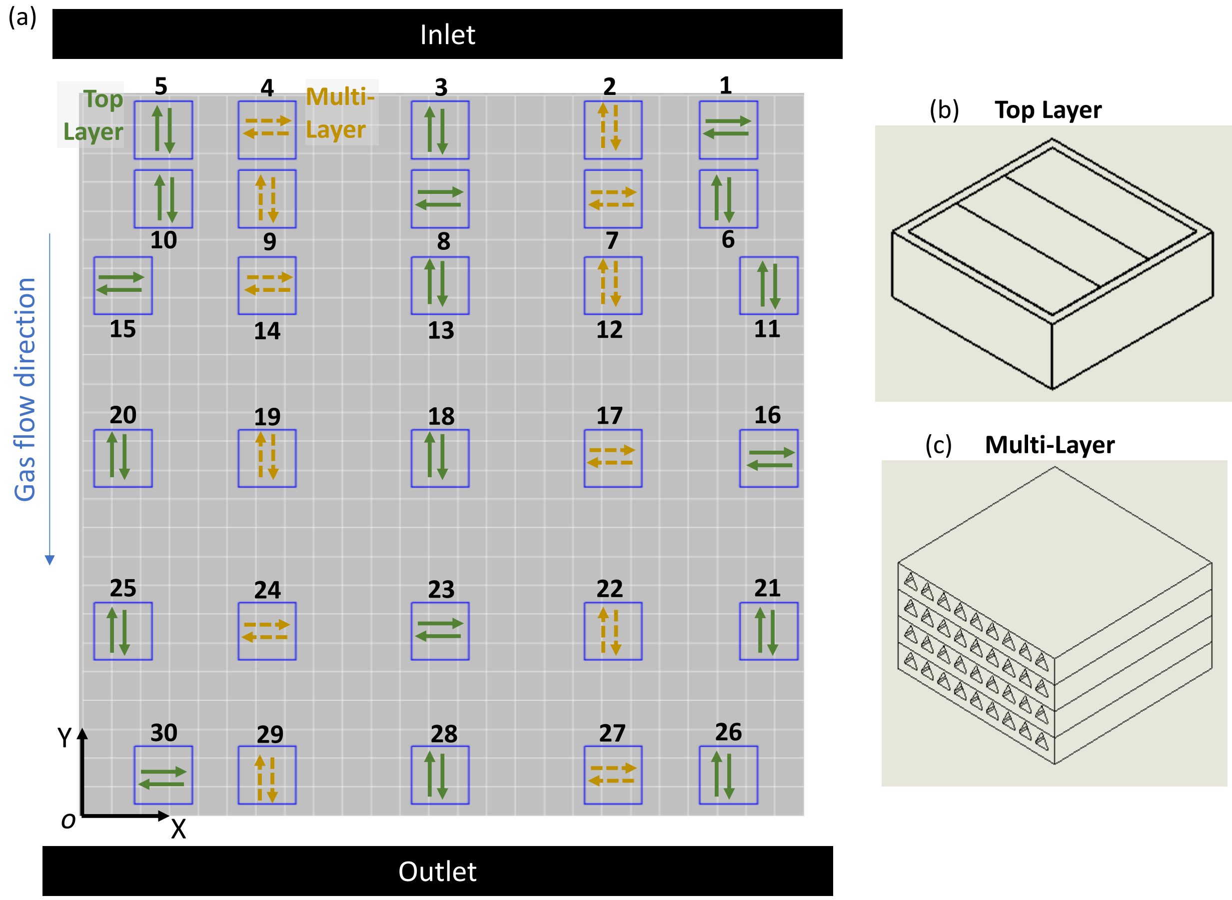

Figure 1. Build layout showing positions of samples, single-track scanning directions (vertical or horizontal), and types of samples (top layer or multi-layer). The origin is denoted with an “*o*” in the lower left corner of the build platform.

Cross-sectioned samples were metallographically prepared. Aqua Regia (1 part nitric acid and 3 parts hydrochloric acid) was used to etch the samples and reveal the melt pool boundaries. Optical micrographs were taken using bright field and dark field imaging with a pixel size of 0.930 µm. Lane et al. (Lane et al., 2020) found the user selection uncertainty (k = 1) in melt pool width and depth measurements was ± 2 pixels and ± 6 pixels, respectively. This results in an uncertainty of 1.86 µm and 5.58 µm, respectively. Representative micrographs for the three different scan speeds are shown in Figure 2. An overview cross-section of a multi-layer sample is shown in Figure 3. There are two single-track laser scans at the bottom of each triangular channel. In some cases, for both top layer and multi-layer samples, there is no melt pool present because it failed to print. Unrelated, single tracks in layer number 2 of multi-layer samples were ignored because of an error in the build file. The melt pool width, height, and area were measured using ImageJ. The width and height were determined by drawing a bounding rectangle around the melt pool. Thus, the width is the widest horizontal distance, and the height is the largest vertical distance that includes both the material above and below the top surface. From here on we use the term height instead of depth since the measurement includes the material above and below the surface. The area was approximated using a polygon tool to outline the melt pool boundary. In the case where multiple melt pool boundaries appear at the bottom of the melt pool (e.g., Figure 2c), the deepest boundary was used.

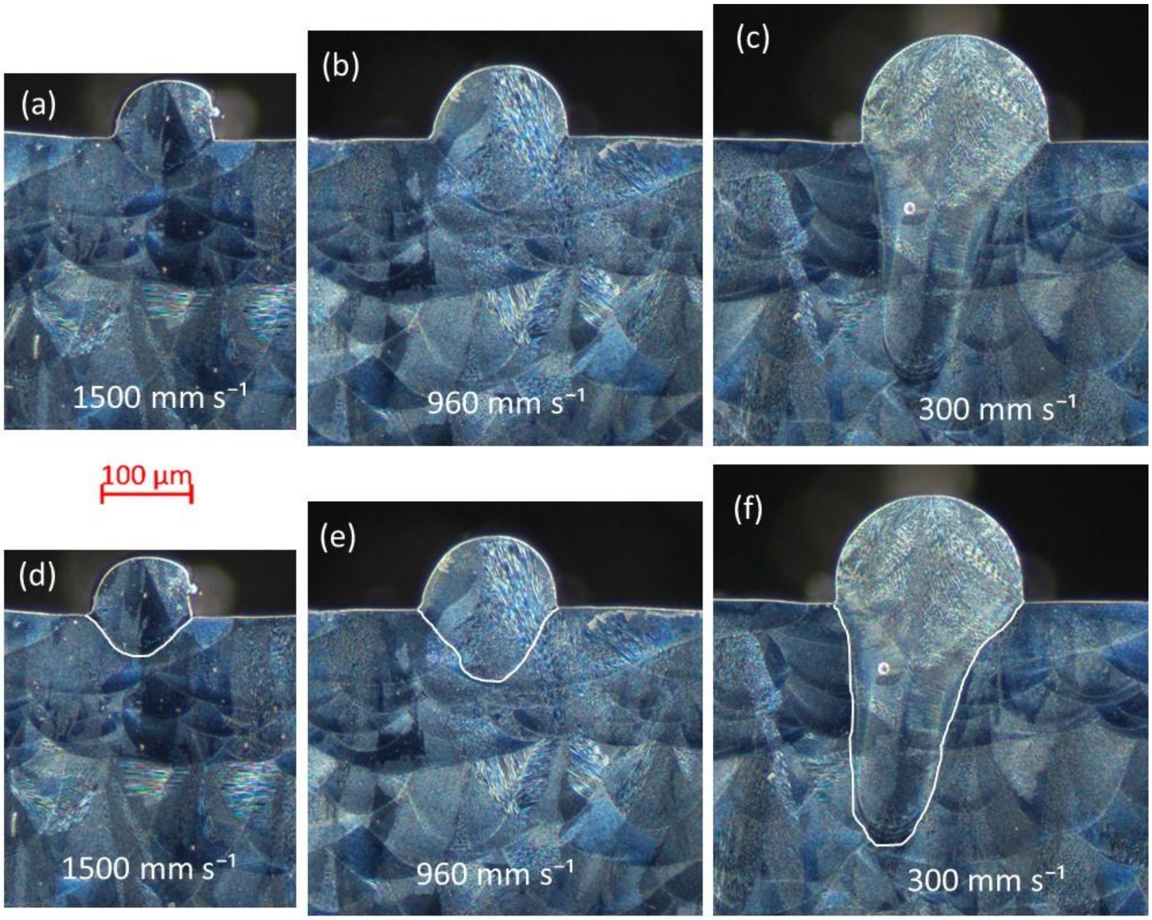

Figure 2. Dark field optical micrographs of cross-sectioned single-track laser scans for (a) 1200 mm s^{-1}, (b) 960 mm s^{-1}, and (c) 300 mm s^{-1}. (d-f) The melt pool boundary is drawn freehand on (a-c) with a white line for emphasis on the bottom row of images. This is for illustration purposes only. See the methods section for a description of the measurement procedure. The sample was etched with Aqua Regia.

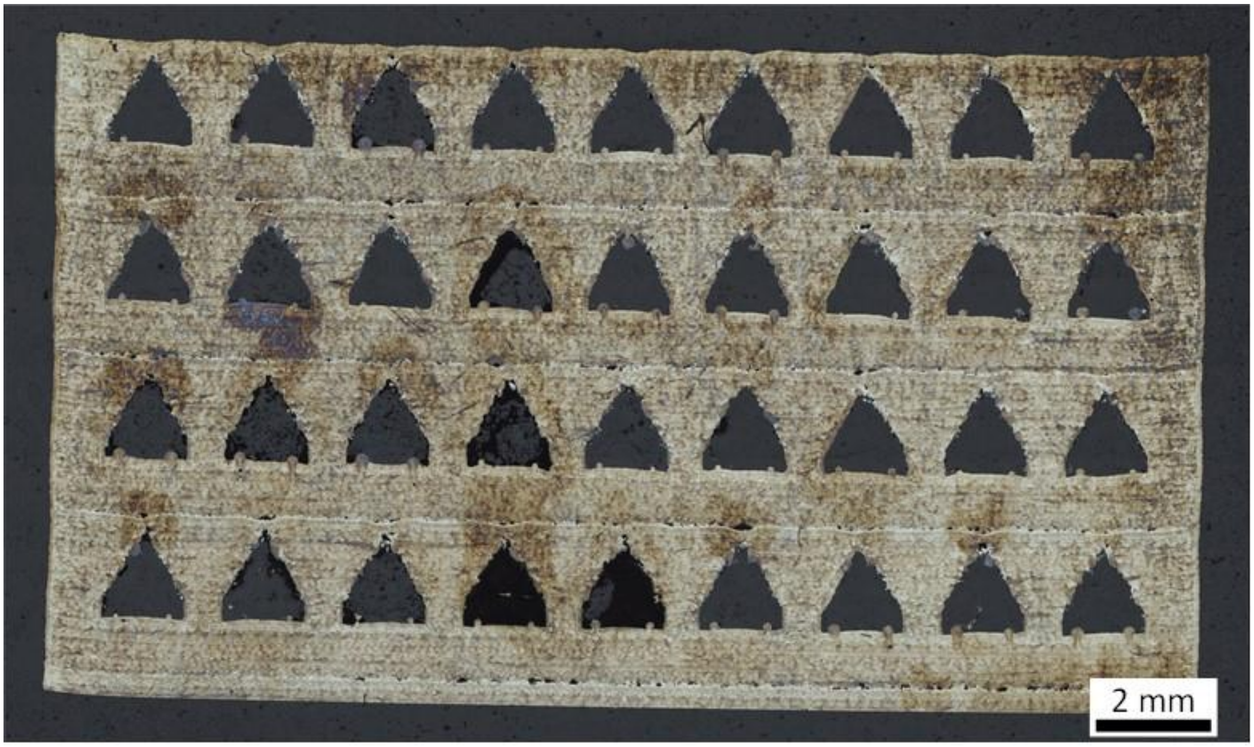

Figure 3. Bright field optical micrograph of cross-sectioned multi-layer sample. There are two single-track laser scans at the bottom of each triangular channel. The sample was etched with Aqua Regia.

Directional inert gas is blown along the -Y-direction in the LPBF machine. There are two inlets (one near the build platform and one positioned on the same wall above the other inlet, near the top of the chamber) and one outlet near the build platform. The gas speed was measured using hot wire anemometers at thirty different positions on the build platform. The anemometers and stage wiring were fed through a modified port cover, and no leaks were detected. The speed profiles at these thirty positions were determined by making 10 measurements along the Z-direction. The maximum speed decreases from the inlet side at approximately 3.5 m s^{-1} to the outlet side at < 2 m s^{-1}. Additionally, the speed profile changes across the build platform as shown in Figure 4. Further details can be found in Ref. (Weaver et al., 2021). Speed measurements were made using nitrogen gas with no powder in the machine compared to the single-track laser scan build that used argon with powder present. The same differential turbine setting of 58 mbar was used for gas speed measurements and the single-track laser scan build. The speed profiles and their non-uniform nature are independent of the gas species, although the average speed may change with different gas species for a fixed differential turbine setting.

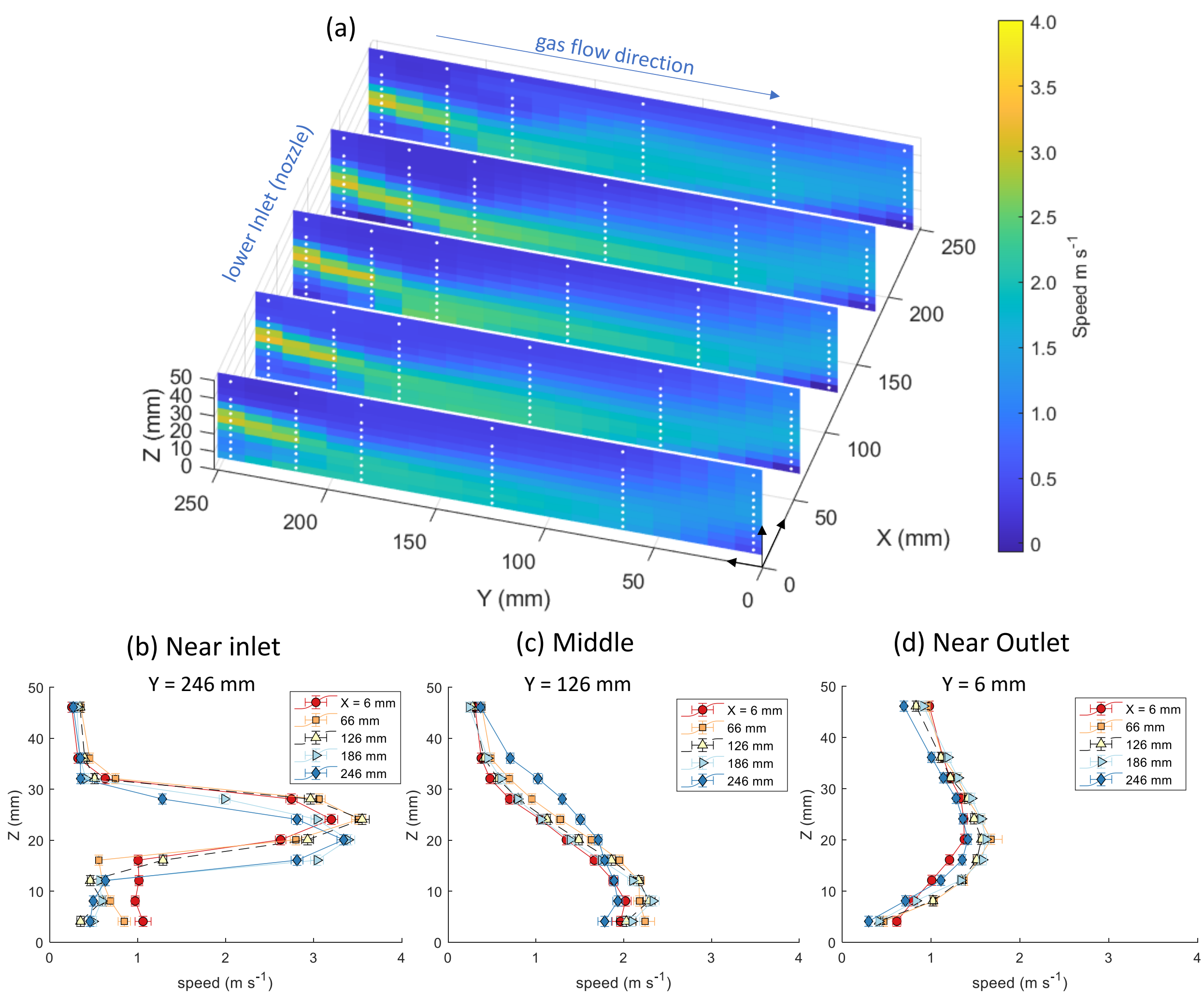

Figure 4. Gas speed measurements with a hot-wire anemometer. (a) interpolation plot for visualization of the speed field based on three hundred measurement points (white dots) and speed profile measurements (b) near the inlet side of the build platform at fixed Y = 246 mm and five different X-positions, (c) in the middle of the build platform at a fixed Y = 126 mm and five different X-positions, (d) near the outlet side of the build platform at a fixed Y = 6 mm and five different X-positions. The gas speed is assumed to be primarily in the -Y-direction. Profile data points are the average ± confidence intervals (p = 68.3%). See Ref. (Weaver et al., 2021) for more details.

3. Results

The build and part characterization resulted in 280 track measurements at three different laser scan speeds (840 in total). The height, width, and area distributions are shown in Figure 5. First, the different scan speeds resulted in distributions about different means, as expected, since the linear heat input (laser power over scan speed) is inversely proportional to laser scan speed. The slowest scan speed of 300 mm s^{-1} results in significantly greater melt pool heights and produced keyhole mode melting based on a depth-to-half-width aspect ratio greater than 1 (see Figure 2). Second, the variation and range in melt pool sizes are incredibly large. The statistics are given in

Table 2. The range (maximum–minimum) is approximately the same as the mean. Some tracks had no melt pool present on the cross-sectional image. This occurred for the fastest scan speed of 1500 mm s^{-1}, which was expected because of the low linear heat input. However, this also occurred for the default scan speed, which was unexpected because these parameters are used to build parts with very low porosity defects. To further illustrate the large variation and range, Figure 6 shows the comparison between tracks produced during the building process (powder on part) and bare plate scans. Single-track laser scans at the default laser power and scan speed on bare plates of a similar alloy (IN718) on the same machine produce mean ± standard deviation (minimum, maximum) depths of 141.3 µm ± 2.7 µm (135.8 µm, 147.0 µm) and widths of 122.4 µm ± 2.1 µm (117.3 µm, 125.7 µm) based on 18 measurements of 9 repeat tracks. Note that there are several other differences: IN625 instead of IN718, 280 measurements instead of 18 measurements, height measurements instead of depth measurements that ignore a small amount of the melt pool that is above the original bare plate surface, and a wide range of track positions and scan directions instead of a small range of track positions and fixed scan direction. Nevertheless, this comparison shows that single tracks created during the building process (powder on part) have a large variation and range compared to single tracks from bare-plate scans. The drawbacks of either approach for studying gas flow effects will be discussed later. Next, we consider how the melt pools vary with Y-position (gas flow direction) and scan direction.

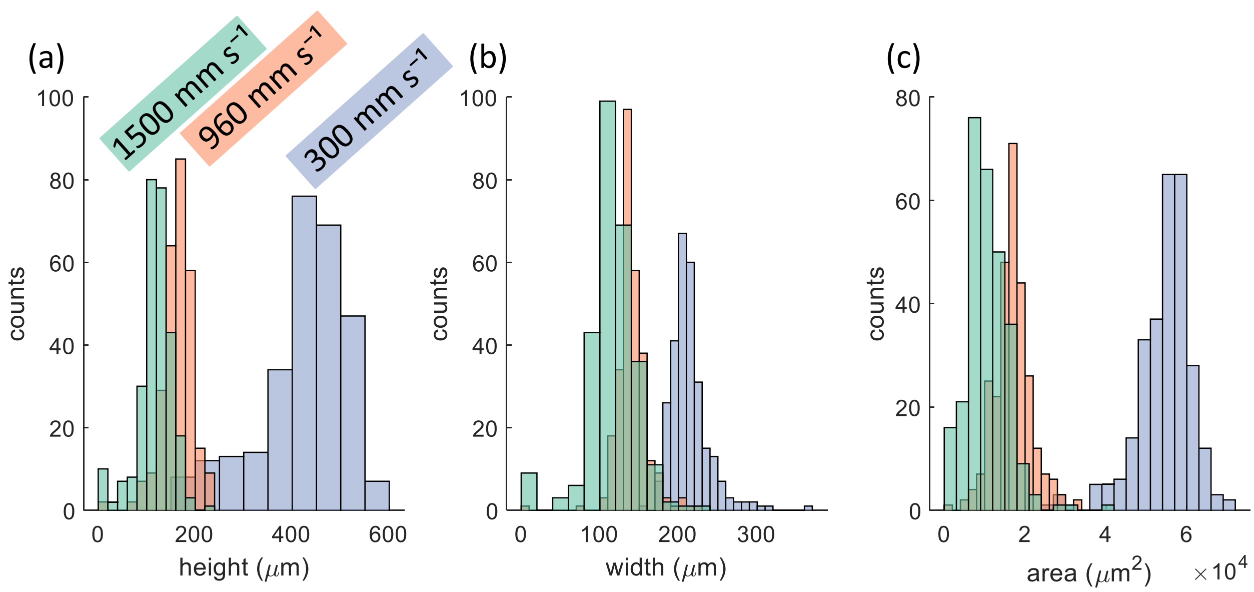

Figure 5. Single-track laser scan melt pool size distributions: (a) height, (b) width, and (c) area. n = 280 per laser scan speed. This includes the top-layer and multilayer samples.

Table 2. Melt pool width and height statistics per scan speed from all the single tracks (n = 280). A value of 0 indicates no track was present on the cross-section.

	Width (μm)				Height (μm)			
Laser Scan Speed (mm s^{-1})	Mean	Std. Dev.	Min.	Max.	Mean	Std. Dev.	Min.	Max.
1500	116.4	32.2	0	234.4	117.1	35.9	0	225.1
960	140.9	19.8	0	226.9	163.9	31.9	0	236.2
300	213.6	24.6	156.7	366.4	424.0	88.4	167.4	574.7

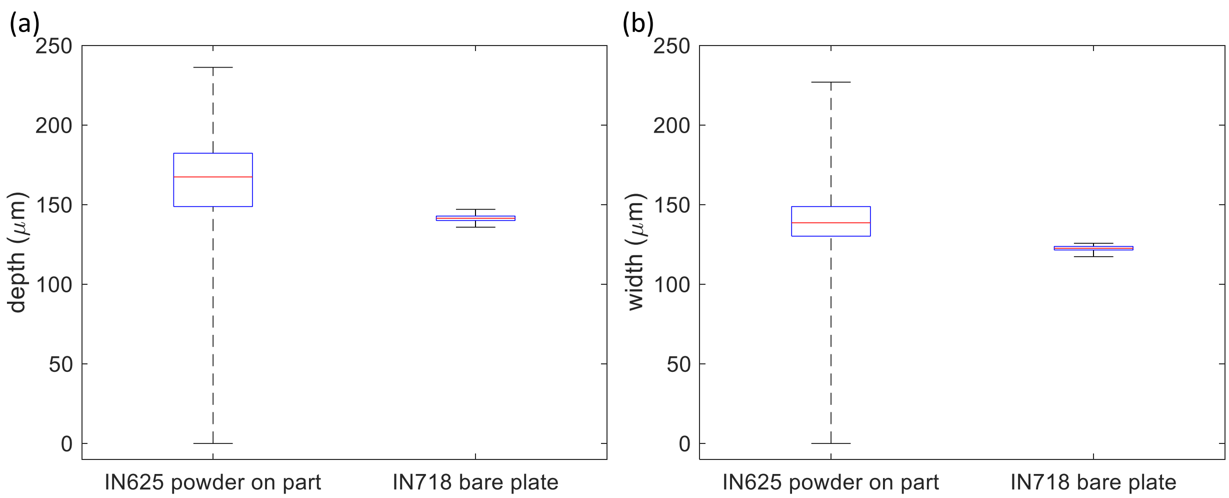

Figure 6. Comparison of single tracks produced during the building process (IN625 powder on part) versus bare plate single tracks (IN718 bare plate). The red line marks the median, the blue box marks the 25th percentile and 75th percent quartiles, and the whiskers are the minimum and maximum values. The determination of outliers was not considered. n = 280 and n = 18 for powder on part and bare plate, respectively.

The directional gas speed profile varied along the Y-direction of the build platform (see Figure 4). Figure 7 shows the melt pool height, width, and area versus Y-position. A Y-position of 0 mm is the edge of the build platform near the outlet side, and conversely, a Y-position of 252 mm is the edge near the inlet side. There were no observable trends in melt pool width and area. The melt pool height decreased near the inlet side of the build platform, and this is most clearly observed in the slowest laser scan speed of 300 mm s^{-1} (Figure 7d). The height data for 960 mm s^{-1} and 1500 mm s^{-1} shows some indication of smaller heights on the inlet side, but they are not as consistent as in the 300 mm s^{-1} data. In other words, the number of data points with overlapping confidence intervals for each scan speed increases with increasing scan speed. Trends with scan direction are presented next.

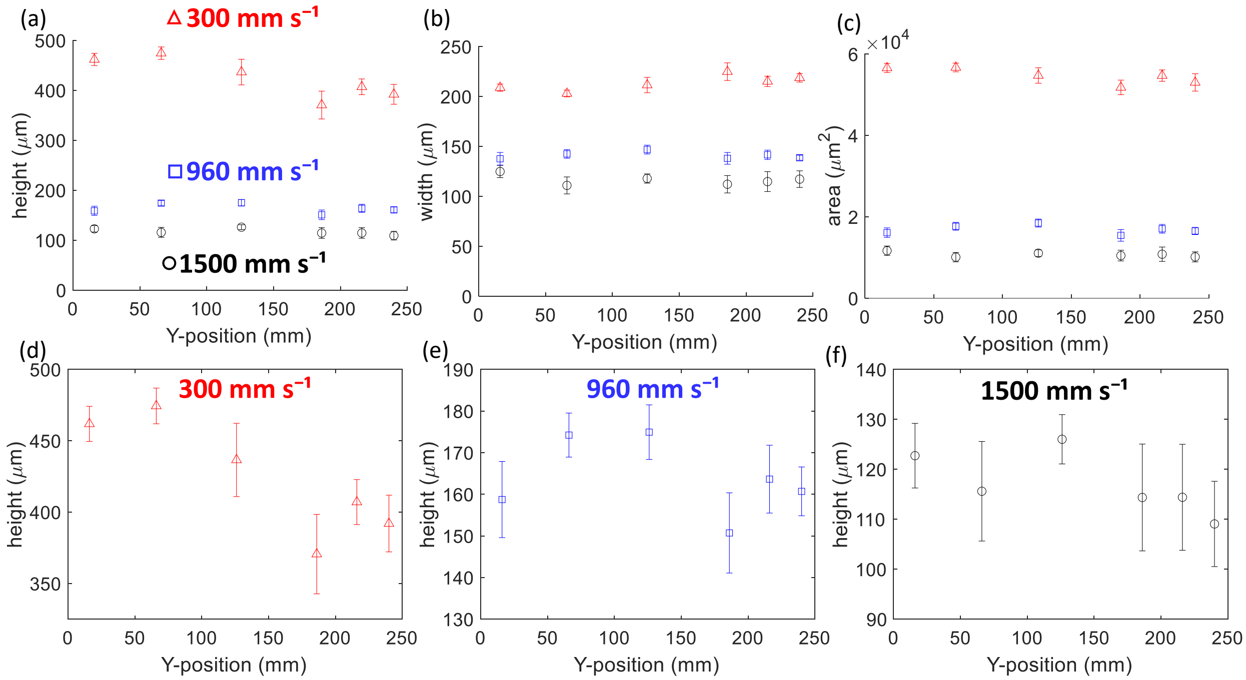

Figure 7. Melt pool measurements with Y-position: (a) height, (b) width, and (c) area. Melt-pool height with Y-position plotted separately for each scan speed (d) 300 mm s^{-1}, (b) 960 mm s^{-1}, and (c) 1500 s^{-1}. Note the different ordinate axis ranges in (d) – (f). Data points are the mean ± 90% confidence interval (n = 46 to 47 per data point).

Figure 8 shows the effect of the scan direction on the melt pool height for the slowest laser scan speed of 300 mm s^{-1}. The laser scan direction was varied with respect to the gas flow direction, shown schematically in Figure 8a. Assuming that plume byproducts are primarily behind the scanning laser when the gas flow and laser scan direction are the same direction (down, -Y), the byproducts are blown back into the laser. The combined effect of the Y-position and laser scan direction can be seen in Figure 8c and d. The difference between scanning down and up is pronounced for Y-positions near the inlet nozzle. Here there is a lower height for the down scan direction. In contrast, there is no difference between the laser scanning left and right, Figure 8d. The left and right scanning tracks follow the overall trend of reduced height near the inlet side of the build platform compared to the outlet side. There were no clear trends with scan direction for the other two laser scan speeds.

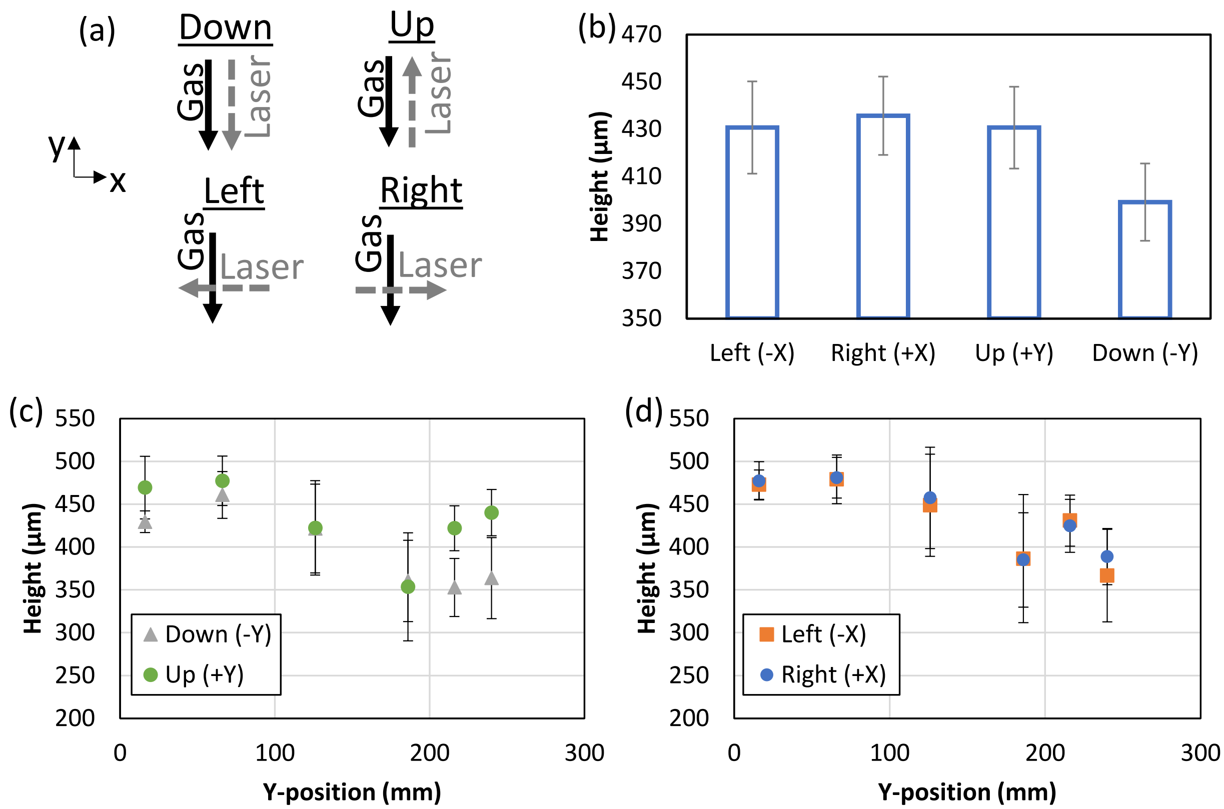

Figure 8. The effect of scan direction on the melt pool height for a laser scan speed of 300 mm s^{-1}. (a) schematic showing how the laser scan direction varies with respect to the gas flow direction, (b) melt pool height with scan direction (n = 66 to 78 per scan direction), (c) melt pool height with Y-position for down and up scan directions (n = 11 to 13 per data point), and (d) melt pool height with Y-position for left and right scan directions (n = 11 to 13 per data point). Data points are the mean ± 90% confidence interval.

4. Discussion

4.1 Single-track melt pool measurements as an indicator

Before discussing the observed trends, it is worth asking whether single tracks created during the building process are a good indicator or tool for studying the effects of gas flow and other process variables. Individual laser scans or welds are the building block of the LPBF process, and single-track laser scans on bare plates are often used for model development due to the well-controlled setup and well-defined boundary conditions (e.g., (Levine et al., 2020)). Single tracks created during the building process are less well controlled because they are built on an AM surface with a full layer of powder. With this added complexity, the single-tracks created during the building process were expected to show higher variance. However, the amount of variance and range that included the absence of a track for some scans was unexpected (see Figure 6). Evidence from this study suggests that single tracks created during the building process may be problematic for drawing definitive conclusions due to the very high variability.

The single tracks, in this case, had a large bead of solid material, much larger than the expected solid layer thickness. The build parameters should produce approximately an average solid layer height of 40 µm since the build platform is lowered this amount each layer. Otherwise, the process would eventually fail due to a lack of fusion or a recoater crash. The bead height (height of material above the previous layer) is much larger for these single tracks. For example, the average height is 92 µm (n = 9) and ranges from 61 µm to 134 µm for the sample located in the center of the build platform. This is 1.5× to 4× the expected value. Shrestha and Chou (Shrestha and Chou, 2018) created single tracks during builds in a similar manner. They observed that the bead height was approximately 3× greater than the expected solid layer thickness, which is consistent with our observations. Yadroitsev and Smurov (Yadroitsev and Smurov, 2011) created three and five track pads (overlapping tracks with alternating scan direction) with powder to study the hatching process. These are referred to as "pad scans" as opposed to single-track scans. They showed that the first track created has a higher bead height than the next track, and the bead height reduces quickly over the first three tracks. The explanation for this behavior is that a track on fresh powder entrains powder from both sides of the track, which feeds the molten pool. In contrast, subsequent tracks that overlap previous tracks have powder available on only one side, and this powder is also the denuded powder region from the prior track. Thus, there is significantly less powder to feed the molten pool. Based on this evidence, a sing laser scan created during the building process is a rare occurrence that is not very representative of the rest of the building process for a typical part.

Single-tracks during the build process were chosen as opposed to a bare plate or a single layer of powder on bare plates in order to create the byproduct environment that occurs during the building process. An effect missing from this experiment is the track-to-track byproduct interaction. Bitharas et al. (Bitharas et al., 2021) showed that some of the byproducts from one track can remain in the atmosphere while the next track is scanning back through. So, during the building process, the laser interacts with the byproducts from the current and previous tracks. This is another deficiency in using single-tracks to study laser-byproduct interactions during the building process. In summary, a single-track created during the building process is a unique track with high variability and increased bead height that may not be indicative of the average process. It is recommended to use pad scans for future experiments because they are more representative of the nominal process.

4.2 Reduced melt pool height

Despite the high variation and identified shortcomings in single-track scans, a reduced melt pool height was observed for the slowest laser scan speed (highest linear heat input). The reduced melt pool height for the slowest scan speed was observed near the inlet nozzle compared to the other half of the build platform (Figure 7). The melt pool height was also reduced when the laser scan direction and gas flow direction were parallel (Figure 8). There are two questions to answer: why was the height reduced, and why did it occur only for the slowest scan speed?

First, the laser incidence angle can be ruled out because it is the same near the inlet and near the outlet, and the height was reduced only near the inlet side of the build platform. In this work, it is assumed that the laser spot size and shape are approximately constant around the build area because the beam waist is positioned within approximately ±1 mm of the build plane. Future work will require confirmation of the spot size and shape around the build plane at operational power, but the following will demonstrate that the most likely cause of melt height variation is related to the difference in gas flow speed profiles across the build platform.

Recall the region near the inlet nozzle has a high maximum speed but low speeds close to the build platform (Figure 4b) compared to a more uniform speed profile across the rest of the build platform. Moran et al. (Moran et al., 2021) created a 2D computational fluid dynamics model of the gas flow in an EOS M290 machine (ignoring the upper inlet diffuser), and they observed that there is a high-velocity laminar eddy in the space between the main jet stream and the build platform on the inlet side of the build platform. It is reasonable to believe this causes poor byproduct removal. The inlet nozzle often develops soot stains during builds despite the high-speed flow, which is another indication that byproducts are recirculated rather than completely removed. The region near the inlet nozzle is upstream from the rest of the build platform so it is not likely that it suffers from the significant spatter accumulation on the powder bed that was reported in downstream regions (see Introduction). Based on these observations, it is likely that the plume byproducts are not removed as efficiently as in other regions of the build platform. This causes beam attenuation and/or scattering and a reduced melt pool height. Reijonen et al. (Reijonen et al., 2020) came to a similar conclusion when the melt pool height decreased during gas flow experiments: inadequate gas velocity caused plume byproducts to remain and attenuate and scatter the laser.

The plume byproducts can also explain the difference in melt pool height when the scan direction and gas flow direction match versus when they are in opposing directions. Figure 8 showed that the melt pool height is reduced when the laser scan direction matches the gas flow direction (down). This is the average result across the whole build platform. In this configuration, the byproducts are blown back into the advancing laser. This is true as long as the plume direction is not primarily in front of the advancing laser. Bidare et al. (Bidare et al., 2018) showed that the plume direction is either toward the laser source or behind the advancing laser for higher linear heat inputs causing larger depressions in the molten pool. It should be noted that the plume direction is stochastic over the track length as seen by Zheng et al. (Zheng et al., 2018). Figure 8 also shows that the reduction in height near the inlet nozzle is diminished when the laser scans antiparallel to the gas flow. This configuration provides the optimal byproduct removal: byproducts are blown away from the advancing laser.

A reduction in melt pool height was not statistically significant for the two faster scan speeds (Figure 5). Zheng et al. (Zheng et al., 2018) demonstrated that byproduct generation is dependent on process parameters. Additionally, Reijonen et al. (Reijonen et al., 2020) showed that the negative effect of a reduction in gas speed on the melt pool height depended on the laser process parameters. Laser parameters with higher linear heat inputs showed a more drastic change from low gas speeds (poor byproduct removal) to high gas speeds (improved byproduct removal). It is possible that some laser parameters are more sensitive to byproduct removal. Finally, (Bitharas et al., 2022) pointed out that when the laser scan speed is slow, the interaction time between the laser and byproduct is greater. This could contribute to why the melt pool height was reduced in some situations for the slowest scan speed.

5. Conclusions

This study aimed to understand the effect of the non-uniform gas flow on the LPBF process by measuring single-track melt pool cross-sections created during the build process with varying laser scan speeds and the scan direction. A reduction in melt pool height associated with poor byproduct removal was dependent on the scan direction, local gas flow profile, and laser process parameters. Improvements to gas flow uniformity and scanning strategies can improve the consistency and quality of LPBF AM. Specifically, the conclusions are as follows:

1. The non-uniform gas flow influences the melt pool height (the distance from the top to the bottom of the melt pool) with reduced heights on one side of the build platform. This corresponded to a region with suspected gas flow eddies that could lead to poor byproduct removal. However, the effect of the non-uniform gas flow was process dependent and most significant at the slowest scan speed (highest linear heat input).
2. Similarly, scan direction influenced melt pool height for only the slowest scan speed. The melt pool height was reduced when the laser scan direction was parallel to the gas flow direction. The difference between scanning parallel and antiparallel to gas flow was pronounced in the region near the inlet nozzle. The reduction in melt pool height near the inlet was lessened when the laser scanned antiparallel to the gas flow.
3. Single-track laser scans printed on parts had highly variable cross-sectional melt pool dimensions with large bead heights. The use of a multilayer sample with channels enabled many more tracks to be printed and characterized. However, the first track printed on undisturbed powder without overlap of neighboring tracks is unique compared to the rest of the printing process. It is recommended to use pad scans to study the melt pool morphology for future studies related to process variation.

Acknowledgements

We would like to thank Mr. Jared Tarr for his technical support for the build. We also wish to acknowledge Dr. Ho Yeung who inspired the design of the multi-layer sample. The authors carried out this work in the course of their official duties as employees of the National Institute of Standards and Technology.

Declaration of Competing Interests

The authors declare they have no conflict of interests.

Appendix A. Detailed breakdown of single-track locations and scan directions.

Table A1. Detailed breakdown of the 280 single-track locations (sample center position), sample type, and scan directions for each scan speed. The same number of tracks were printed for each scan speed on each sample number unless otherwise noted with the scan speed in parenthesis. These differences arose from unforeseen behavior in the print setup software. Refer to Figure 1 for the coordinate system and sample numbers.

Sample No.	X (mm)	Y (mm)	Sample Type	No. of +X tracks	No. of -X tracks	No. of +Y tracks	No. of -Y tracks
1	226	240	Top Layer	2	2	0	0
2	186	240	Multi-layer	0	0	9	9
3	126	240	Top Layer	0	0	2 (300, 1500); 1 (960)	1 (300, 1500); 2 (960)
4	66	240	Multi-layer	9	9	0	0
5	30	240	Top Layer	0	0	2 (300, 1500); 1 (960)	1 (300, 1500); 2 (960)
6	226	216	Top Layer	0	0	2	2
7	186	216	Multi-layer	9	9	0	0
8	126	216	Top Layer	2	2	0	0
9	66	216	Multi-layer	0	0	9	9
10	30	216	Top Layer	0	0	2 (300, 1500); 1 (960)	1 (300, 1500); 2 (960)
11	240	186	Top Layer	0	0	2 (300, 1500); 1 (960)	1 (300, 1500); 2 (960)
12	186	186	Multi-layer	0	0	9	9
13	126	186	Top Layer	0	0	2 (300, 1500); 1 (960)	1 (300, 1500); 2 (960)
14	66	186	Multi-layer	0	0	9	9
15	16	186	Top Layer	2	2	0	0
16	240	126	Top Layer	2	2	0	0
17	186	126	Multi-layer	0	0	9	9
18	126	126	Top Layer	0	0	2 (300, 1500); 1 (960)	1 (300, 1500); 2 (960)
19	66	126	Multi-layer	0	0	9	9
20	16	126	Top Layer			2	2
21	240	66	Top Layer	0	0	2 (300, 1500); 1 (960)	1 (300, 1500); 2 (960)
22	186	66	Multi-layer	0	0	9	9
23	126	66	Top Layer	2	2	0	0
24	66	66	Multi-layer	0	0	9	9
25	16	66	Top Layer	0	0	2	2
26	226	16	Top Layer	0	0	2	2
27	186	16	Multi-layer	0	0	9	9
28	126	16	Top Layer	0	0	2 (300, 1500); 1 (960)	1 (300, 1500); 2 (960)
29	66	16	Multi-layer	0	0	9	9
30	30	16	Top Layer	2	2	0	0

Figure A1. Schematic showing the distribution of laser scan speeds for each channel in the multi-layer sample. Each channel contains a pair of ±y or ±x tracks depending on the sample orientation. Note the second row of channels from the bottom was not included due to an error in the printing setup file. In other words, only 18 tracks per scan speed were measured for each multi-layer sample.

Appendix B. Base material printing parameters

The single-track printing parameters are provided in the main text (Table 1). The inskin and upskin parameters are listed here because these are relevant to the base material on which all of the single tracks were printed. The terminology is consistent with EOSPrint software. The laser spot diameter (D4σ) is estimated to be approximately 80 µm.

Table B1. Inskin parameters. "Distance" is more commonly known as hatch spacing. The scan rotation is based on hatching parameters X, Y, alternating, and rotated all being selected. The layer thickness pertains to the nominal solid layer thickness.

Parameter type	Power (W)	Speed (mm/s)	Distance (mm)	Stripe Width (mm)	Stripe Overlap (mm)	Layer thickness (µm)	Beam offset (mm)	Scan rotation
Inskin	285	960	0.11	10	0.08	40	0.015	67°

Table B2. Upskin parameters. The thickness refers to the distance from the top surface when the upskin parameter starts (i.e., it is applied to the top three layers of the part). The upskin parameter scans the part twice on each layer: first in a manner consistent with the inskin scan rotation, and second with a rotation that is perpendicular to the first scan rotation.

Parameter type	Laser Power (W)	Scan Speed (mm/s)	Distance (mm)	Overlap w/ inskin (mm)	Minimum length (mm)	Thickness (mm)
Upskin	153	600	0.09	0.10	0.10	0.12

References

AHMED OBEIDI, M., MUSSATTO, A., GROARKE, R., VIJAYARAGHAVAN, R. K., CONWAY, A., ROSSI KASCHEL, F., MCCARTHY, E., CLARKIN, O., O'CONNOR, R. & BRABAZON, D. 2020. Comprehensive assessment of spatter material generated during selective laser melting of stainless steel. *Materials Today Communications,* 25**,** 101294.

ANWAR, A. B. & PHAM, Q.-C. 2017. Selective laser melting of AlSi10Mg: Effects of scan direction, part placement and inert gas flow velocity on tensile strength. *Journal of Materials Processing Technology,* 240**,** 388-396.

BEREZ, J., SHERIDAN, L. & SALDAÑA, C. 2022. Extreme variation in fatigue: Fatigue life prediction and dependence on build volume location in laser powder bed fusion of 17-4 stainless steel. *International Journal of Fatigue,* 158**,** 106737.

BIDARE, P., BITHARAS, I., WARD, R. M., ATTALLAH, M. M. & MOORE, A. J. 2018. Fluid and particle dynamics in laser powder bed fusion. *Acta Materialia,* 142**,** 107-120.

BITHARAS, I., BURTON, A., ROSS, A. J. & MOORE, A. J. 2021. Visualisation and numerical analysis of laser powder bed fusion under cross-flow. *Additive Manufacturing,* 37**,** 101690.

BITHARAS, I., PARAB, N., ZHAO, C., SUN, T., ROLLETT, A. D. & MOORE, A. J. 2022. The interplay between vapour, liquid, and solid phases in laser powder bed fusion. *Nature Communications,* 13**,** 2959.

DEISENROTH, D. C., NEIRA, J., WEAVER, J. & YEUNG, H. Effects of Shield Gas Flow on Meltpool Variability and Signature in Scanned Laser Melting. ASME 2020 15th International Manufacturing Science and Engineering Conference, 2020. V001T01A017.

ESMAEILIZADEH, R., ALI, U., KESHAVARZKERMANI, A., MAHMOODKHANI, Y., MARZBANRAD, E. & TOYSERKANI, E. 2019. On the effect of spatter particles distribution on the quality of Hastelloy X parts made by laser powder-bed fusion additive manufacturing. *Journal of Manufacturing Processes,* 37**,** 11-20.

FERRAR, B., MULLEN, L., JONES, E., STAMP, R. & SUTCLIFFE, C. J. 2012. Gas flow effects on selective laser melting (SLM) manufacturing performance. *Journal of Materials Processing Technology,* 212**,** 355-364.

GRESES, J., HILTON, P. A., BARLOW, C. Y. & STEEN, W. M. 2004. Plume attenuation under high power Nd:yttritium–aluminum–garnet laser welding. *Journal of Laser Applications,* 16**,** 9-15.

LADEWIG, A., SCHLICK, G., FISSER, M., SCHULZE, V. & GLATZEL, U. 2016. Influence of the shielding gas flow on the removal of process by-products in the selective laser melting process. *Additive Manufacturing,* 10**,** 1-9.

LANE, B., HEIGEL, J., RICKER, R., ZHIRNOV, I., KHROMSCHENKO, V., WEAVER, J., PHAN, T., STOUDT, M., MEKHONTSEV, S. & LEVINE, L. 2020. Measurements of melt pool geometry and cooling rates of individual laser traces on IN625 bare plates. *Integrating Materials and Manufacturing Innovation***,** 1-15.

LEVINE, L., LANE, B., HEIGEL, J., MIGLER, K., STOUDT, M., PHAN, T., RICKER, R., STRANTZA, M., HILL, M. & ZHANG, F. 2020. Outcomes and conclusions from the 2018 AM-Bench measurements, challenge problems, modeling submissions, and conference. *Integrating Materials and Manufacturing Innovation,* 9**,** 1-15.

MORAN, T. P., WARNER, D. H., SOLTANI-TEHRANI, A., SHAMSAEI, N. & PHAN, N. 2021. Spatial inhomogeneity of build defects across the build plate in laser powder bed fusion. *Additive Manufacturing,* 47**,** 102333.

NASSAR, A. R., GUNDERMANN, M. A., REUTZEL, E. W., GUERRIER, P., KRANE, M. H. & WELDON, M. J. 2019. Formation processes for large ejecta and interactions with melt pool formation in powder bed fusion additive manufacturing. *Scientific Reports,* 9**,** 5038.

REIJONEN, J., REVUELTA, A., RIIPINEN, T., RUUSUVUORI, K. & PUUKKO, P. 2020. On the effect of shielding gas flow on porosity and melt pool geometry in laser powder bed fusion additive manufacturing. *Additive Manufacturing,* 32**,** 101030.

SHCHEGLOV, P. Y., GUMENYUK, A. V., GORNUSHKIN, I. B., RETHMEIER, M. & PETROVSKIY, V. N. 2012. Vapor–plasma plume investigation during high-power fiber laser welding. *Laser Physics,* 23**,** 016001.

SHEN, H., ROMETSCH, P., WU, X. & HUANG, A. 2020. Influence of Gas Flow Speed on Laser Plume Attenuation and Powder Bed Particle Pickup in Laser Powder Bed Fusion. *JOM,* 72**,** 1039-1051.

SHRESTHA, S. & CHOU, K. 2018. Single track scanning experiment in laser powder bed fusion process. *Procedia Manufacturing,* 26**,** 857-864.

TENBROCK, C., KELLIGER, T., PRAETZSCH, N., RONGE, M., JAUER, L. & SCHLEIFENBAUM, J. H. 2021. Effect of laser-plume interaction on part quality in multi-scanner Laser Powder Bed Fusion. *Additive Manufacturing,* 38**,** 101810.

WEAVER, J., SCHLENOFF, A., DEISENROTH, D. & MOYLAN, S. P. 2021. Inert Gas Flow Speed Measurements in Laser Powder Bed Fusion Additive Manufacturing. *Advanced Manufacturing Series (NIST AMS).* Gaithersburg, MD: National Institute of Standards and Technology.

YADROITSEV, I. & SMUROV, I. 2011. Surface Morphology in Selective Laser Melting of Metal Powders. *Physics Procedia,* 12**,** 264-270.

YOUNG, Z. A., GUO, Q., PARAB, N. D., ZHAO, C., QU, M., ESCANO, L. I., FEZZAA, K., EVERHART, W., SUN, T. & CHEN, L. 2020. Types of spatter and their features and formation mechanisms in laser powder bed fusion additive manufacturing process. *Additive Manufacturing,* 36**,** 101438.

ZHENG, H., LI, H., LANG, L., GONG, S. & GE, Y. 2018. Effects of scan speed on vapor plume behavior and spatter generation in laser powder bed fusion additive manufacturing. *Journal of Manufacturing Processes,* 36**,** 60-67.